fortuitous or to be expected; obviously, they confirm the theory put forward in the present article. They suggest that the final strategy to optimize criterion (14) will certainly take advantage of the established algorithms used in current direct methods.

The authors are grateful to C. Lemaréchal, J. C. Gilbert and Professor E. E. Castellano for very valuable suggestions and criticisms.

References

COLLINS, D. (1978). *Acta Cryst.* A34, 533-541.
DECARREAU, D., HILHORST, D., LEMARÉCHAL, C. & NAVAZA, J. (1992). *SIAM* (*Soc. Ind. Appl. Math.*) *J. Optim.* In the press.
DE TITTA, G. T., LANGS, D. A., EDMONDS, J. W. & DUAX, W. L. (1980). *Acta Cryst.* B36, 638-645.
FERCHAUX, Y., VILLAIN, F. & NAVAZA, A. H. (1990). *Acta Cryst.* C46, 346-348.
FREY, M., LEHMANN, M., KOETZLE, T. & HAMILTON, W. (1973). *Acta Cryst.* B29, 876-884.
GOEDKOOP, J. A. (1950). *Acta Cryst.* 3, 374-378.
KARLE, J. (1971). *Acta Cryst.* B27, 2063-2065.
KARLE, J. & HAUPTMAN, H. (1950). *Acta Cryst.* 3, 181-187.
MAIN, P., FISKE, S. J., HULL, S. E., LESSINGER, L., GERMAIN, G., DECLERCQ, J.-P. & WOOLFSON, M. M. (1980). *MULTAN80. A System of Computer Programs for the Automatic Solution of Crystal Structures from X-ray Diffraction Data.* Univs. of York, England, and Louvain, Belgium.
NAVAZA, A. H., SCHWEISS, P., ALZARI, P., CHEVRIER, G., HEGER, G. & GUIDA, J. (1990). *J. Solid State Chem.* 89, 23-30.
NAVAZA, J. (1986). *Acta Cryst.* A42, 212-223.
NAVAZA, J. & SILVA, A. M. (1979). *Acta Cryst.* A35, 266-275.
SAYRE, D. (1952). *Acta Cryst.* 5, 60-65.
SCHWARTZ, L. (1966). *Théorie des Distributions*, p. 116 Paris: Hermann.
SIKKA, S. K. (1969). Thesis, Bombay Univ., India.
TSOUCARIS, G. (1970). *Acta Cryst.* A26, 492-499.

Acta Cryst. (1992). A48, 700-716

3D Structure Determination from Electron-Microscope Images: Electron Crystallography of Staurolite

BY H.-R. WENK

University of California, Department of Geology and Geophysics, Berkeley, CA 94720, USA

K. H. DOWNING

Lawrence Berkeley Laboratory, Donner Laboratory, Berkeley, CA 94720, USA

HU MEISHENG

University of California, Department of Geology and Geophysics, Berkeley, CA 94720, USA

AND M. A. O'KEEFE

Lawrence Berkeley Laboratory, National Center for Electron Microscopy, Berkeley, CA 94720, USA

(*Received 9 October 1991; accepted 31 March 1992*)

Abstract

Resolution of better than 2 Å has been obtained in many crystals by high-resolution electron microscopy. Although this resolution is sufficient to resolve interatomic spacings, structures are traditionally interpreted by comparing experimental images with contrast calculations. A drawback of this method is that images are 2D projections in which information is invariably obscured by overlap of atoms. 3D electron crystallography, developed by biophysicists to study proteins, has been used to investigate the crystal structure of staurolite. Amplitudes and phases of structure factors are obtained experimentally from high-resolution images (JEOL ARM 1000 at the National Center for Electron Microscopy at LBL), taken in different directions from thin regions where dynamic scattering is minimal. From images in five orientations (containing 59 independent reflections to a resolution of 1.38 Å), a 3D electron potential map is constructed which resolves clearly all cations (Al, Si, Fe, including those with partial occupancy) and all O atoms. This method has great potential in crystal structure determinations of small domains in heterogeneous crystals which are inaccessible to X-ray analysis. It is estimated that 3D structure determinations should be possible on regions only about ten unit cells wide and should resolve not only atom positions but also site occupancies. The method is also applicable to space-group determination.

0108-7673/92/050700-17$06.00 © 1992 International Union of Crystallography

1. Introduction

With improvement in electron-microscope design, point-to-point resolution sufficient to resolve interatomic spacings has been obtained in many materials (*e.g.* Smith *et al.*, 1985; Gronsky, 1980). Although individual atoms may be resolved under favorable conditions, determination of the crystal structure from the images is seldom straightforward. Traditionally, two-dimensional images are obtained for a range of thickness and focus, and a series of experimental images is then compared with contrast calculations based on the multibeam dynamical theory (*e.g.* O'Keefe, Buseck & Iijima, 1978). This technique has been applied to minerals, and it was possible in several examples to interpret features not only of the crystal structure but also of defects. The study of biopyriboles (Veblen & Buseck, 1979) is an excellent example. One drawback of this method is that it provides only two-dimensional projections of the structure, and in those projections information is invariably lost due to the superposition of atoms at different levels in the unit cell in the beam direction. With resolution of 1.5 Å, as is available in some microscopes, it should be possible to resolve single atoms which are typically spaced 2–3 Å, if we could obtain a three-dimensional (3D) deconvolution of the information contained in high-resolution images. The basic necessary information is not contained in a single image but in a combination of images which view the structure in different directions. Biophysicists have developed such a method to investigate the structure of proteins (De Rosier & Klug, 1968; De Rosier & Moore, 1970).

This so-called electron crystallography resembles an X-ray structure determination in which the crystal structure is reconstructed by a Fourier synthesis from amplitudes and phases of diffracted waves (*e.g.* Glaeser, 1985). For X-rays, the phase cannot be measured directly and various direct and indirect methods have been developed to determine phases from amplitudes (*e.g.* Stout & Jensen, 1989). However, if images of the structure are available, such as obtained with a high-resolution electron microscope, phases and amplitudes of diffracted waves can be obtained directly from the Fourier analysis of the image. Information on phases and amplitudes from several images, representing different views of the specimen, is combined and then Fourier transformed to a three-dimensional map of the Coulomb potential of the crystal.

In the case of proteins, resolution is limited by several factors, mainly related to the sensitivity of organic materials to damage by the electron beam. The limited exposure which the specimen can tolerate results in images which are statistically noisy, requiring that large image areas be analyzed in order to obtain a sufficient signal-to-noise ratio (SNR). The large unit cell of most protein crystals and relatively high temperature factors reduce diffraction amplitudes, particularly at high resolution, making recovery of data from images even more difficult. Only recently was the structure of the first protein determined successfully by electron crystallography. A model for the structure of the membrane protein bacteriorhodopsin was derived from electron-microscopy data with a resolution approaching 3.5 Å (Henderson *et al.*, 1990) which is still not sufficient to image single atoms. The same method should be applicable to minerals for which much higher point-to-point resolution can be obtained than for proteins. However, a condition is that dynamic scattering is minimal so that the weak-phase-object approximation is valid.

We have chosen the mineral staurolite as a test example. The structure is well known (*e.g.* Smith, 1968) and moderately complex with light and heavy atoms, cations in octahedral and tetrahedral coordination, and partial occupancy of some of the sites. Atoms are close packed with Si–O distances of less than 1.7 Å, thus putting a high demand on resolution. Staurolite occurs naturally in large crystals, and preliminary electron-microscopy observation indicated that it was homogeneous and stable in the beam which made it suitable for a test case. We could observe sections cut in different directions without having to worry about possible variations in structure from one area to the next.

In the following sections we will describe first the conventional method of image analysis, based on comparison of experimental images with dynamic contrast calculations. This is done to investigate the influence of thickness, focus and dynamic scattering on image contrast, and on phases and amplitudes of diffracted waves. We describe then, in some detail, the procedure of electron crystallography for 3D structure determination. Preliminary results have been reported earlier (Downing, Hu, Wenk & O'Keefe, 1990). The method is at this point quite demanding in instrumentation and software and has to rely on interdisciplinary collaboration, but this has been one of the rewarding aspects of the project. The conventional method, which requires knowledge of a structure model, is not a prerequisite for 3D electron crystallography.

2. Description of staurolite

The basic structure of staurolite was first determined by Náray-Szabó (1929). This nearly orthorhombic mineral can be described as a cubic close packing of oxygen with Al occupying octahedral interstices and Si and Fe occupying tetrahedral interstices. There is a close structural relationship with kyanite, with which staurolite is frequently intergrown. Based on chemical analyses (*e.g.* Jacob, 1941; Juurinen, 1956)

and a reinvestigation of the structure (Náray-Szabó & Sasvári, 1958), an idealized structural formula $HFe_2Al_9Si_4O_{24}$ was established. On the basis of weak reflections in X-ray diffraction patterns, the space group $C2/m$ was determined with only very minor deviations from the orthorhombic space group *Ccmm*. More recent refinements of the structure (Hainisch, 1966; Smith, 1968) proved that the previous model was basically correct but provided more data about the cation distribution and the location of H atoms (Takéuchi & Aikawa, 1972). In this paper we use the structure model of Smith (1968, Table 2, p. 1144) as a basis. However, we mapped his monoclinic coordinates into an orthorhombic unit cell. Atomic displacements from monoclinic symmetry are less than 0.02 Å, too small to cause any concern for electron crystallography. Specifically for image simulation and representation we used space group *Ccmm* ($a = 7.82$, $b = 16.52$ and $c = 5.63$ Å), a setting of *Cmcm* (No. 63 in *International Tables for Crystallography*, 1989), in order to maintain a correspondence with the true monoclinic space group $C2/m$ in which the mineral is traditionally described.

3. Experimental techniques

Thin foils were prepared from petrographic thin sections by ion-beam thinning with Ar^+ ions accelerated to 5 kV and a beam current of 1 mA. Specimens were then coated with a thin film of carbon to prevent charging. After preliminary investigation with a conventional transmission electron microscope, atomic resolution imaging and diffraction were conducted with the JEOL ARM 1000 at the National Center for Electron Microscopy (NCEM), Lawrence Berkeley Laboratory. The atomic resolution microscope (ARM) is designed to optimize high-resolution imaging and has a reproducible point-to-point resolution of less than 1.6 Å (Hetherington, Nelson, Westmacott, Gronsky & Thomas 1989). The ARM operates at voltages ranging from 400 to 1000 kV. The product $C_s\lambda$ remains constant over the range of possible incident electron wavelengths (λ), so that Scherzer defocus is constant for all operating conditions (−544 Å). Throughout this study, a voltage of 800 kV was used, which gives a spherical aberration coefficient (C_s) of 1.93 mm. Imaging was conducted with an objective aperture which includes beams with lattice spacings greater than 0.83 Å. Images were viewed on a TV monitor, which was indispensable for aligning the microscope. Through-focus series of images in increments of 80 or 120 Å were recorded on film at 500 000× magnification. Astigmatism was corrected at the minimum contrast defocus condition and the slight dependence of astigmatism on focus in the ARM was ignored. All data were taken from the thinnest areas at the edge of the specimen in order to minimize dynamical scattering effects.

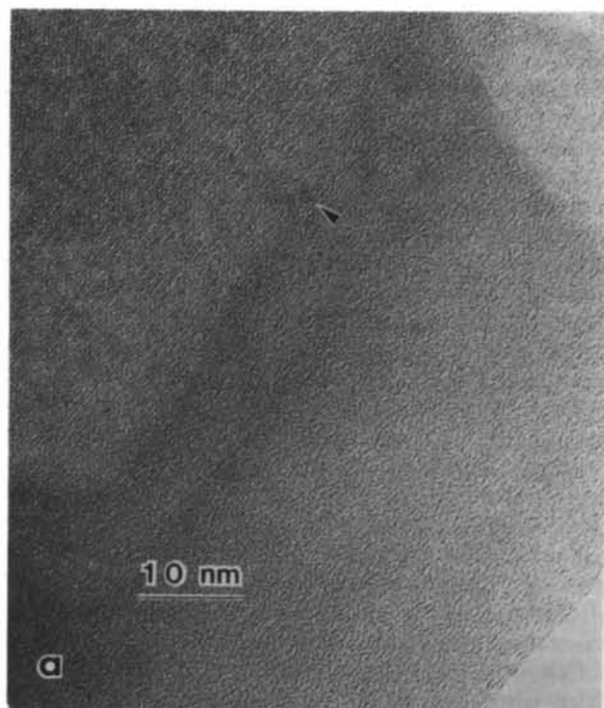

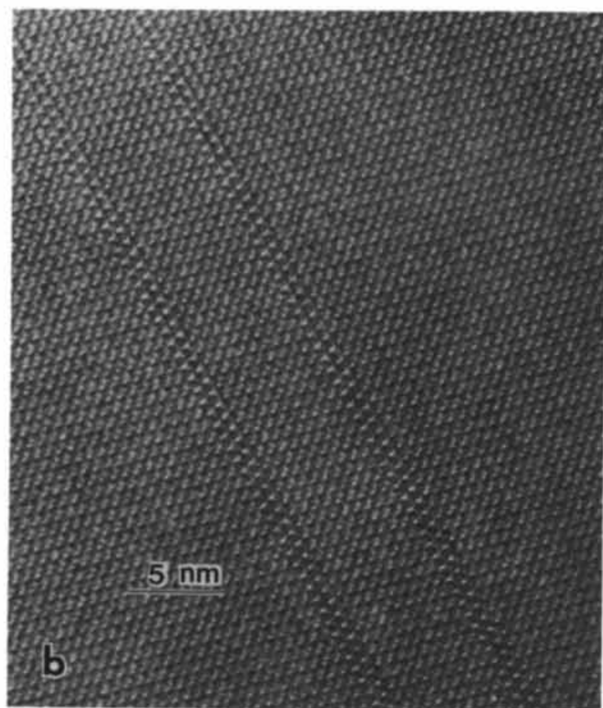

Fig. 1. (*a*) ARM image of staurolite illustrating the edge of the foil with amorphous material and crystal structure in the thicker part of the foil. The region from which structural data were obtained is indicated by an arrow. (*b*) Stacking faults in kyanite, topotactically intergrown with staurolite. Notice faults and microtwins.

Fig. 1(*a*) is a typical image of the foil. Note the amorphous layer, which is best visible near the edge of the foil, and was produced during ion-beam thinning. Lattice fringes and structural details are well visible in the thicker parts of the foil. The staurolite crystal is very homogeneous, with only a few defects. Locally there are topotactic intergrowths of staurolite with kyanite which are easily recognized even on a macroscopic scale. Kyanite displays stacking faults and twins (Fig. 1*b*) which have been reported previously (Wenk, 1980). Experimental images were obtained in five directions. For this we used three orthogonal sections to obtain [100], [010] and [001] images, and applied the high-angle (±40°) double-tilt stage to obtain [101] and [310] images from the [100] specimen. Portions of these images used for the electron crystallography analysis are shown in Fig. 2(*a*).

The images were examined on an optical diffractometer to assess general quality, *i.e.* defocus, astigmatism, crystal orientation and resolution. Very often the foil is slightly bent near the edge which turned out to be one of the major limitations with these data. Small portions of the original 500 000× negatives were selected and digitized on a Perkin-Elmer PDS 1010M microdensitometer in 400 × 400 pixel arrays with a 25 μm sampling distance corresponding to 0.5 Å on the specimen. The digitized image was Fourier transformed into a diffraction pattern. For small thicknesses there is considerable noise in the images. This is partially due to limited statistics but mainly to scattering from the amorphous layer (Fig. 1). This nonperiodic noise can be eliminated by Fourier filtering of digitized experimental images, using only waves corresponding to the staurolite lattice. As in previous applications to minerals (*e.g.* Meike, Wenk, O'Keefe & Gronsky, 1988), the appearance of such a Fourier filtered image (Fig. 2*b*) is vastly improved over that recorded on the film (Fig. 2*a*).

4. Conventional image analysis

Because dynamical scattering effects are often significant, the electron wave leaving the specimen may not be a simple representation of the projection of the specimen structure. In addition, the transfer of information to the image is not perfect due to limitations of the microscope. For thin specimens, this transfer can be described with the linear-image contrast transfer function (CTF); examples are shown in Fig. 3 for the ARM 1000 operated at 800 kV for three focus conditions (Hetherington *et al.*, 1989). For Scherzer focus the envelope of the CTF (dashed line) approaches zero at $d = 1.6$ Å, which determines the highest resolution up to which image interpretations are straightforward. The image recorded on film is the convolution of the scattered waves with the Fourier transform of the CTF.

Interpretation of images relies on a comparison of experimental images with simulated images based on a model for the crystal structure and dynamic contrast calculations. We have used the *NCEMSS* suite of programs (Kilaas, 1987) to simulate images for staurolite. These programs simulate an electron microscope consisting of an electron beam, a specimen and a lens system. The incident electron beam is idealized as consisting of parallel plane wave electrons within the specimen and the lens system as a single spherically aberrated objective lens. The operator furnishes a model crystal structure [in our case based on the atomic parameters determined by Smith (1968)] and the specification of the real microscope lens system, including the parameters describing the CTF. A qualitative match for different focus and thickness has been considered as good evidence that the structure model is correct.

Fig. 4 compares a simulated thickness–focus series and an experimental focus series for the zone axis [001]. For small thicknesses, agreement over the whole focus series is satisfactory. Fig. 2 compares experimental images in the five orientations used in this study (Fig. 2*a*) with corresponding image simulations for Scherzer focus and a thickness of 50 Å (Fig. 2*c*).

Unfortunately, such a procedure does not enable us to assess the quality of the model structure quantitatively. There is no way analytically to derive a model from the image. Furthermore, the image corresponds to a 2D projection of the structure that introduces superpositions of atom images, which can be particularly severe for ionic structures with tight bonding in coordination polyhedra. For example, imaging of oxygen in most oxides would require a point-to-point resolution of 1.2 Å (Epicier, O'Keefe & Thomas 1990) which has only recently become available in a very few laboratories.

In Fig. 5 we compare experimental selected-area diffraction patterns (SAD) obtained in each of the three main directions, averaging over an area of 5000 Å in diameter, with diffractograms obtained by optical diffraction with a laser from a small area of interest in the image. The diffractogram is affected by the CTF, the SAD is not. In the diffractograms (Fig. 5*c*) we observe a diffuse ring which is due to scattering from the amorphous layer. It can be used to assess astigmatism (in the case illustrated for [001] the image is slightly astigmatic) and to estimate focus (at Scherzer focus the ring is most diffuse and extends to small *d* spacing). The experimental diffraction patterns are compared with simulated SAD's and diffractograms. We notice overall agreement, but there are a number of reflections with amplitudes which are visibly different. For example, 200 has a high intensity in the diffraction pattern and is almost absent in the simulation. We attribute this largely to dynamic effects in the experimental diffraction

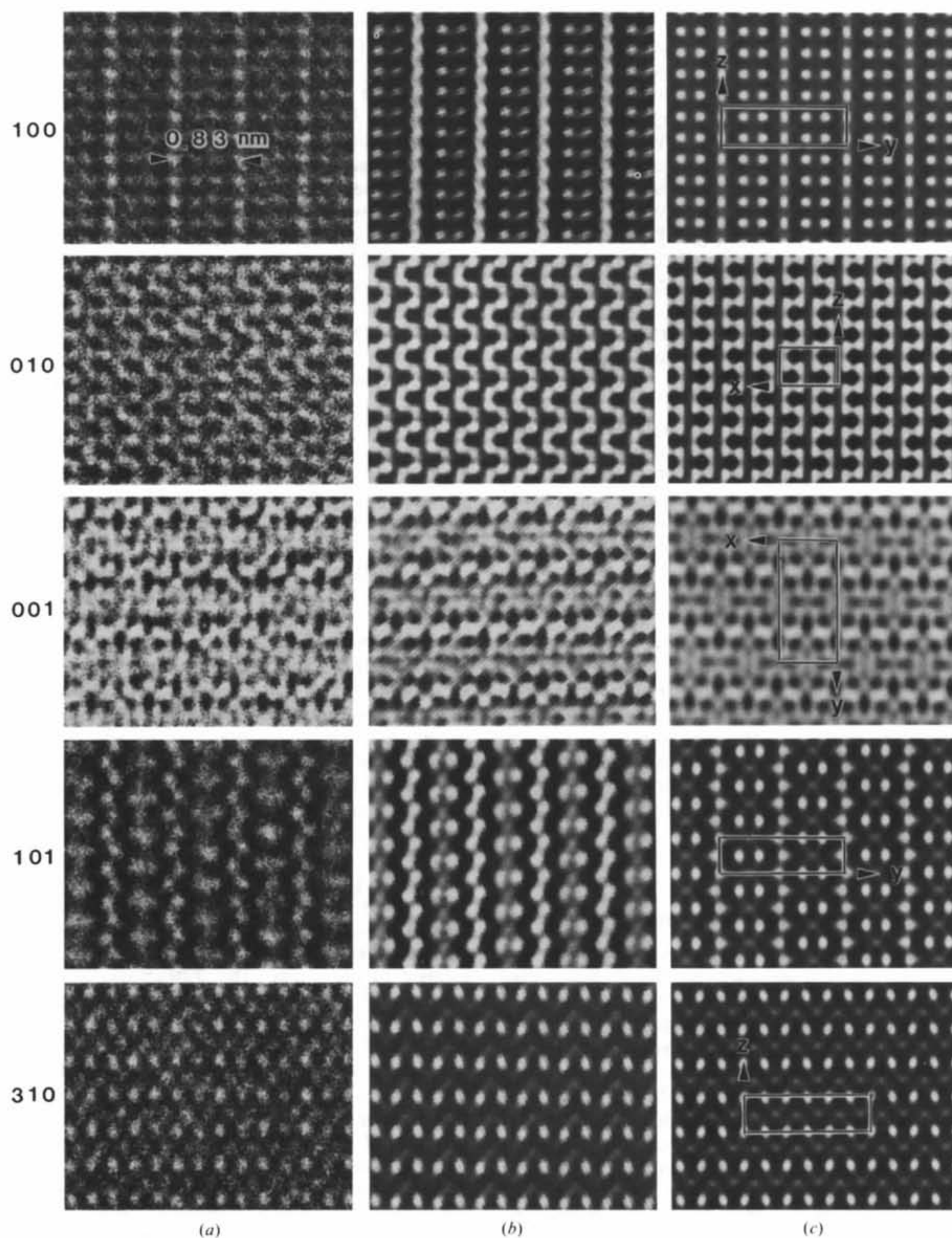

Fig. 2. High-magnification phase contrast images in the five sections used in this study (Scherzer focus). (*a*) Experimental image on film. (*b*) Processed experimental image with only the periodic contribution but not imposing symmetry. (*c*) Dynamical contrast simulation based on Smith's (1968) model for conditions of the ARM 1000 operated at 800 kV, Scherzer focus and a thickness of 50 Å.

pattern which averages over a large specimen area including thicknesses over 200 Å, whereas the simulated pattern is for a thin foil of 30 Å thickness. Also, bending over this large area could introduce some intensity into this reflection. The intensity shown at the 200 position in both the experimental and computed diffractograms (*i.e.* the image intensity spectra) is the sum of all diffracted-beam interferences between pairs of beams differing in position by this vector (including any 000–200 interference), but does not require any explicit contribution from the 200 diffracted beam in the image amplitude spectrum to produce it.

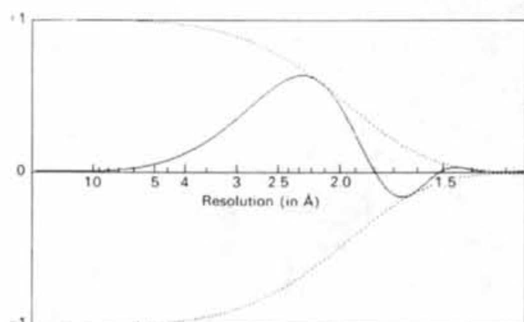

(*a*)

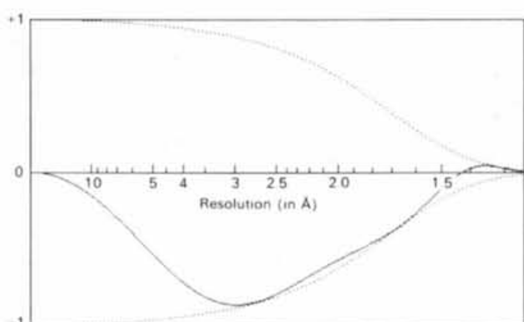

(*b*)

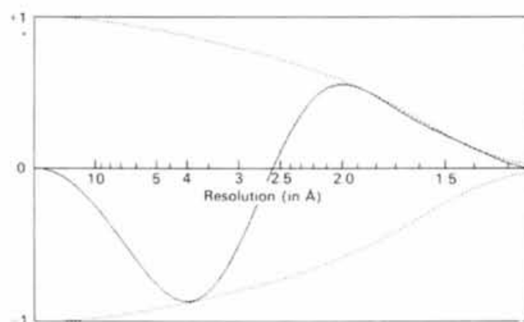

(*c*)

Fig. 3. Linear-image contrast transfer function (CTF) curves for the JEOL ARM-1000 for three defocus values at 800 kV: (*a*) zero defocus (Gaussian focus); (*b*) −500 Å (near Scherzer); (*c*) −800 Å. As the degree of underfocus is increased from (*a*) through (*c*), the damping envelope (dashed line) allows the CTF (solid line) to transfer more of the higher spatial frequencies into the image. Curves are plotted for a C_s value of 1.93 mm, a convergence semiangle of 0.8 mrad and a Gaussian spread of focus of 120 Å halfwidth.

Fig. 6(*a*) uses computations for several reflections to illustrate that amplitudes vary linearly with thickness up to 50 Å. Above that thickness (Fig. 6*b*), changes become more complex due to dynamic scattering and excitation error and cannot be directly interpreted. In the centrosymmetric case phases derived from images are less affected by dynamical effects but depend upon specimen thickness, microscope defocus and resolution. Phase shifts occur at larger changes in thickness and focus. Phase changes with thickness are due to dynamic interaction and occur at different thicknesses for different reflections. Phase changes due to focus (Fig. 6*c*) are described by the CTF (Fig. 3) and depend upon the resolution of the reflection as well as the amount of microscope defocus. Since the specimen areas that have been analyzed are well under 100 Å thick, a kinematic approximation is justified, but contributions from dynamic scattering introduce errors which will be discussed below.

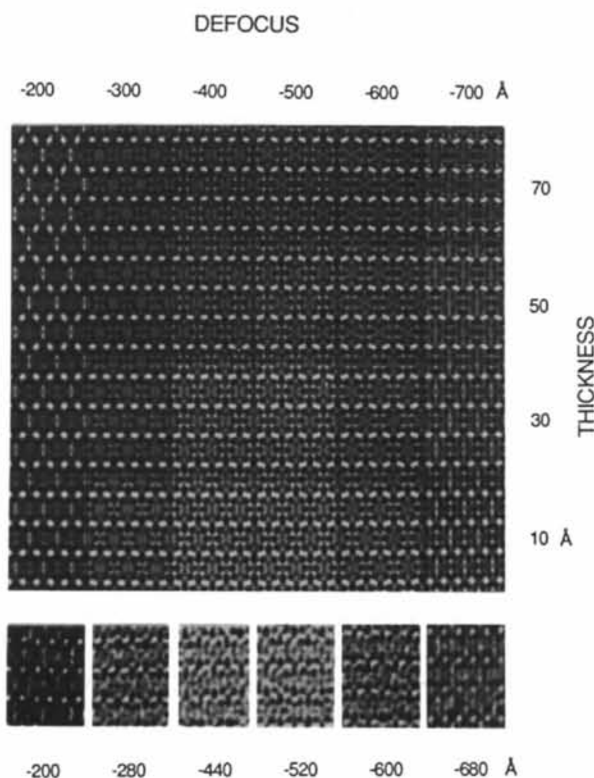

Fig. 4. Simulated dynamical thickness–focus contrast series of [001] images of staurolite (top) compared with experimental focus series (bottom).

Fig. 5. Diffraction patterns in the three main lattice directions. (*a*) Experimental selected-area diffraction patterns (SAD) with convergent beam on an area of 5000 Å in diameter on the specimen at conditions of the atomic resolution imaging. (*b*) Simulated SAD for a sample thickness of 30 Å. (*c*) Diffractograms obtained by laser diffraction on an optical bench from the experimental ARM image on an area of 150 Å in diameter. The diffuse ring pattern is due to the contribution from the amorphous part and illustrates astigmatism for [001]. (*d*) Simulated diffractograms for a thickness of 30 Å. Relative to (*b*) there is a drop off in intensity with resolution due to the CTF.

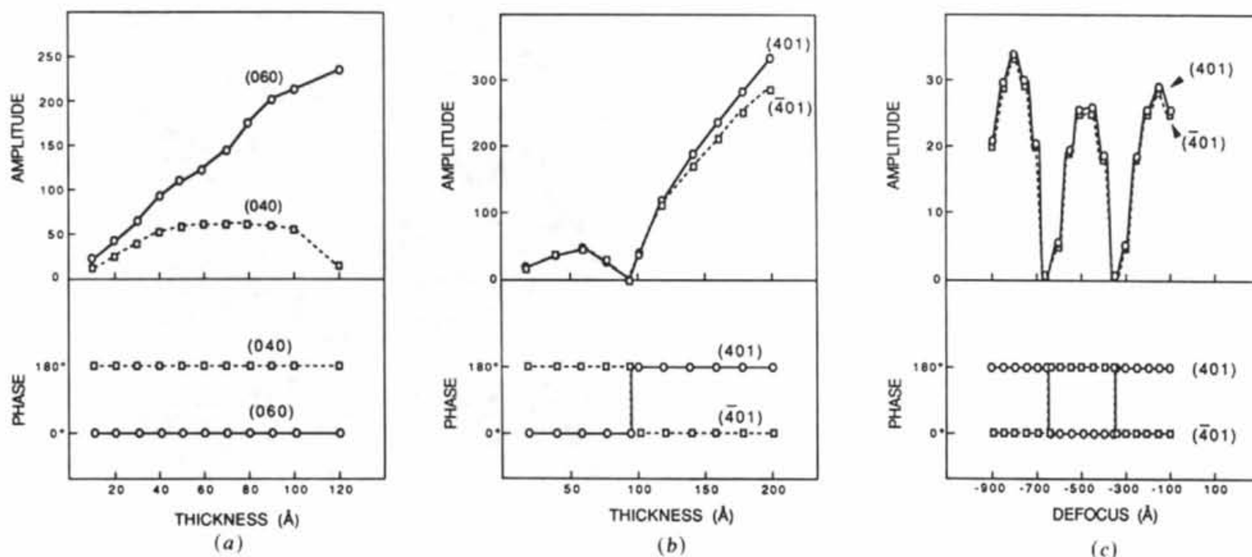

Fig. 6. Variations of amplitudes and phases with thickness (*a*), (*b*) and focus (*c*) for selected reflections based on dynamic multibeam simulations. Reflections 401 and $\bar{4}01$ are symmetry related. Phase changes with focus are due to the CTF.

5. Electron crystallography

We restrict our attention to the case where the specimen is thin enough that single-scattering approximations are valid, so that the image can be assumed to be a linear representation of the specimen. The Fourier transform of each projection then provides a central section of the reciprocal lattice. Combining a sufficient number of different sections gives data which fill the 3D reciprocal space densely enough to allow calculation of the 3D real-space Coulomb potential by Fourier transformation. All of our computer processing of the data used codes derived from the program suite of the MRC [Medical Research Council, Cambridge, England (Amos, Henderson & Unwin, 1982)].

(a) *Structure-factor determination*

As described above, images are digitized into 400 × 400 pixel arrays and Fourier transformed. With the transform displayed on a computer graphics screen, the reciprocal lattice can be indexed to define the location of all diffraction spots. The indexing of these 2D projection images is independent of the indexing of the 3D data, but the 2D-to-3D transformation must be determined. The Fourier transform is described by the expression

$$F_{HK} = \iint B(X, Y) \times \exp\left[2\pi i(HX + KY)\right] \mathrm{d}X \, \mathrm{d}Y \qquad (1)$$

where F_{HK} is the structure factor for the reciprocal-lattice spot HK and $B(X, Y)$ is the film density at the position X, Y. All relevant information about the crystal structure is contained in the structure factors for integer reciprocal-lattice positions HK. The remaining values of the Fourier transform are noise, introduced mainly from the amorphous layer and by poor counting statistics. The structure-factor amplitudes and phases are extracted from the transform, correcting for the local background in the transform mainly produced by the amorphous contribution. The unit-cell image in the projection is then calculated from these structure factors by an inverse Fourier transform.

(b) *Phase-origin determination*

Because the origin of the scanned area does not generally coincide with the origin of the unit cell, the image reconstructed from these structure factors will not be centered. The unit-cell origin is usually chosen at a point of high symmetry, *i.e.* the intersection of several symmetry axes, in accordance with conventions defined for example in *International Tables for Crystallography* (1989). Only with this origin will the structure-factor phases obey the symmetry rules for the structure. The process of phase-origin determination searches through the unit cell for the position with the best agreement between the observed phases of symmetrically equivalent structure factors and the known (or presumed) symmetry constraints. Shifting the image to the proper origin is in fact done by applying the appropriate phase shifts to the structure factors in reciprocal space. A measure of the quality of the data is given by the agreement of the phases, after origin refinement, with the symmetry constraints.

All five of the projections used in this work are centrosymmetric, so that all phases should be 0 or 180°. In addition, the sections [001, 101, 100] have mirror planes, so that phases (as well as amplitudes) must obey $F_{HK} = F_{H\bar{K}}$. The sections [010, 310] have glide planes, which requires $F_{HK} = F_{H\bar{K}}$ or $F_{HK} = F_{H\bar{K}} - \pi$, depending on H and K. The phase constraints used in the phase-origin search were those of the 2D plane group $p222$ for [001, 101, 100] and $p21$ for [010, 310].

The presence of several symmetry axes in the unit cell gives several possible choices for the phase origin. The correct one is selected by specifying a set of reference phases when they are available. In the case of a new structure, the origin may be chosen arbitrarily among points of highest symmetry in the first orientation. The origin is then constrained in subsequent orientations by the reflections which occur in both orientations. In this work we used a subset of three to five of the phases from the model calculations to establish the same phase origin for both the model and experimental data, in order to allow direct comparisons.

(c) *Correction for contrast transfer function (CTF)*

The CTF modulates both the amplitude and the phase of structure factors determined from the image. There are two components to the CTF, as shown in Fig. 3. The envelope of the CTF, arising mainly from the limited spatial and temporal coherence of the illumination, decreases high-resolution contrast in a way that can be analytically described (Frank, 1973) as

$$E(u) = \exp\{-\tfrac{1}{2}\pi^2\lambda^2\Delta^2u^4\} \times \exp\{-\pi^2\alpha^2(\varepsilon + C_s\lambda^2u^2)^2u^2\} \qquad (2)$$

where λ is the wavelength of the incoming electron beam, Δ is the spread of focus due to energy spread in the electron beam (and any instabilities in the microscope high voltage or lens current), α is the semi-angle of incident-beam convergence (half the angle subtended by the condenser lens at the specimen), ε is defocus, C_S is the spherical aberration coefficient and u is the reciprocal-space coordinate (O'Keefe, 1979).

The component arising from defocus and spherical aberration modulates the amplitudes and can also flip phases by 180° (see Fig. 6c):

$$F_{\text{image}} = F_{\text{specimen}} \sin(\chi),$$

where

$$\chi = \pi\varepsilon\lambda u^2 + \tfrac{1}{2}\pi C_S\lambda^3 u^4. \quad (3)$$

At Scherzer focus the CTF (Fig. 3*b*) has the same sign throughout most of the range of resolution and thus provides the most easily interpreted image. In our earlier work (Downing *et al.*, 1990) we selected the image from each focus series that appeared closest to Scherzer focus. A significant problem, however, is to determine which image is at Scherzer focus or, more generally, to determine the defocus for any image, particularly in the cases where the foil is tilted. In the case of amorphous films (and proteins, where the large unit cell gives a high density of diffraction spots), the Fourier transform of the image will be modulated by rings representing zeros of the CTF. These rings, though, have very low amplitude at resolution beyond about 2–3 Å and are thus of little help at the highest resolution.

We have utilized the variation in amplitude with defocus, as shown in Fig. 6(*c*), by attempting to match the diffraction amplitude from the images in the focal series to CTF values for a series of six to ten images. This approach has used an adaptation of the MRC program *CTFREFINE*, which performs a least-squares fit between a set of electron diffraction amplitudes for the specimen and the image amplitudes that would arise with a given defocus. Since reliable electron diffraction amplitudes were not available for the small specimen areas we considered here, the highest amplitude for each reflection, F_{HK}, found in the whole focus series was used as a reference amplitude (assuming that $|\sin\chi|$ is approximately unity for any reflection at the defocus condition yielding the maximum amplitude for that reflection). The modified program (*CTFSERIES*) then varied the starting focus (as well as astigmatic focus difference and azimuth) to find the best match between these reference amplitudes modified by a CTF and the observed amplitudes for all reflections in the whole focus series.

Table 1. *Changes in amplitudes and phases as a function of focus*

Shown for two selected pairs of symmetry-related reflections of staurolite for the whole focus series going from underfocus to overfocus in 80 Å steps. Phases are corrected for the sign of the CTF which is indicated but not yet shifted to a correct phase origin. Notice fair agreement between phases except for weak reflections. The highest amplitude of the through-focus series was chosen for the reconstruction.

110 $d = 7.11$ Å (11) in [001]

	(11)			$(1\bar{1})$		
Film no.	Amplitude	Phase	CTF	Amplitude	Phase	CTF
394	2831.9	14.8	−	5217.5	175.7	−
395	1968.1	−68.8	−	2338.3	167.6	−
396	4187.2	6.1	−	2715.4	−172.9	−
397	5250.5	14.1	−	4202.9	−178.8	−
398	5423.9	6.1	−	4722.4	165.4	−
399	5712.1	4.8	−	5054.5	171.7	−
400	4317.1	10.5	−	5359.5	180.0	−
401	3514.4	−16.3	−	4782.8	171.0	−

133 $d = 1.74$ Å (31) in [310]

	(31)			$(3\bar{1})$		
Film no.	Amplitude	Phase	CTF	Amplitude	Phase	CTF
134	1736.4	−71.2	−	2932.9	59.0	−
145	5004.3	−179.5	+	4444.5	18.6	+
136	7551.1	−156.4	+	8585.2	29.3	+
137	6103.1	−122.2	−	3700.5	−0.7	−
138	3672.6	−129.0	−	10293.9	9.6	−
139	5804.3	−150.3	−	5696.0	29.6	−

This procedure enables us to determine structure factors from each image of the focus series. Two examples, one for low and one for high resolution, are shown in Table 1. After CTF correction and phase-origin determination, each measurement of a particular (HK) should give the same phase, which is in general the case, except for weak reflections such as (11) on film 395 and (31) on film 134 which deviate more than 50° from the mean of the rest. The two reflections in the pairs of Table 1 ($11/1\bar{1}$ and $31/3\bar{1}$) are symmetry related and are expected to have phases different by 180°. Statistical errors in phase measurement can then be reduced by combining all measurements, using an appropriate weighting scheme which takes advantage of the quality of each of the measurements (Brillinger, Downing & Glaeser, 1990). At this stage we also combined data from symmetry-related reflections whose phases should be the same. The reproducibility of the measurements is reflected in a figure of merit (FOM) which is calculated as

$$\mathrm{FOM}_{HK} = \sum w_i F_{HK,i} \Big/ \sum |F_{HK,i}| \quad (4)$$

where w_i is the weight assigned to the measurement of F_{HK} in the ith image. The weights are based on the peak-to-background ratio for each reflection, calculated to give the smallest r.m.s. error in the resulting map.

Using images outside Scherzer focus not only gives better confidence in assigning Scherzer focus, but allows us to determine the sign of the CTF for some of the measured reflections at resolutions outside the first CTF zero at Scherzer focus (Table 1). There is still some error in determining the defocus, so that reflections close to a CTF zero may suffer a phase error of 180°. Within the focus series, though, the consensus phase is generally well determined by reflections far from the zeros. We have been able to include most reflections in the five projections to 1.38 Å resolution in the present work.

Another consideration is the falloff of the envelope function which attenuates amplitudes at high resolution. A density map calculated with the reduced amplitudes for high-resolution reflections will have the appearance of a lower-resolution image. Dividing the structure-factor amplitudes from the images by the value calculated from (2) should give a better approximation to the electron diffraction amplitudes than is obtained directly from the images, and should enhance high-resolution details in the reconstruction as will be shown later in Fig. 9. However, one problem

is the relative contribution of non-linear interference terms, and there is thus the possibility that boosting the high-resolution amplitudes will introduce errors in the map and reduce its interpretability. Plotting the ratio of experimental *versus* calculated amplitudes, we see that the data for the raw images (Fig. 7*a*) roughly follow the form of the envelope function. We then divided the amplitudes by the envelope function calculated with the form of (2), but limiting the maximum amplitude increase to a factor of ten. The plot of the ratio of corrected experimental to calculated amplitudes (Fig. 7*b*) now shows essentially no resolution dependence, although there is quite a bit of scatter of the ratio. It thus appears that we introduce no spurious detail by compensating for the envelope.

(*d*) *Data merging*

Finally, the 2D *HK* indices for each projection are converted to 3D *hkl* indices, and data from the five projections are combined to produce the 3D data in the unique octant of the 3D reciprocal space. For each projection, a scale factor was determined from the average ratio of the observed amplitudes to the amplitudes calculated from the model. One could also take any of the projections as a reference and scale the other projections to it by using the common reflections. Phases were determined from a weighted average of the phases determined from different projections, using the FOM as the weight.

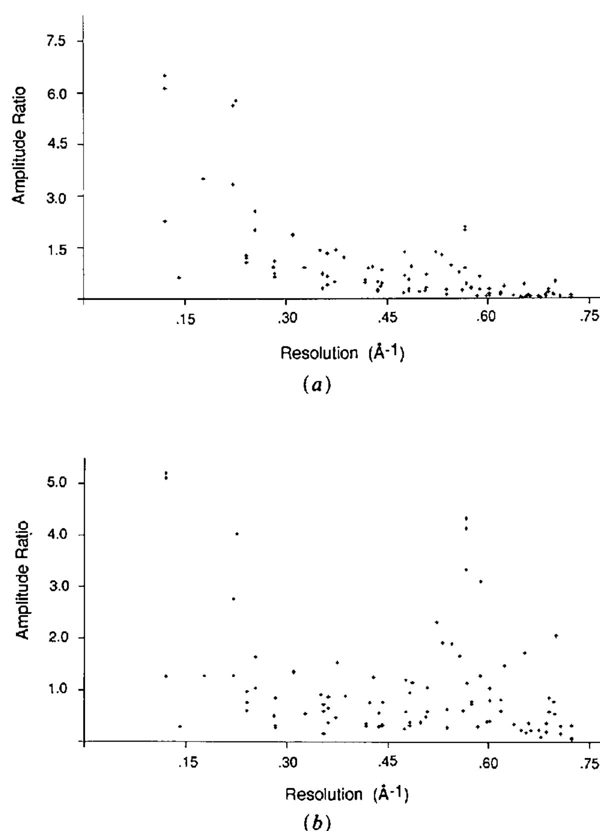

Fig. 7. (*a*) Ratio of experimental and calculated amplitudes as a function of resolution. Note the large scatter and the systematic drop off with resolution which results from the CTF. (*b*) After correction for the envelope of the CTF the average ratio shows little dependence on resolution.

6. Results: 3D model

Experimental values for amplitudes and phases of structure factors are shown in Table 2, which includes the averaged values from each focus series for each projection and the resultant overall average, as well as the values calculated from the model structure. The table contains measurements for 59 unique reflections, out of a total of a possible 93 non-extinct reflections to 1.38 Å; of these, 50 out of 74 possible reflections fall within the resolution range to 1.5 Å, with an additional 9 out of 19 within the range from 1.5 to 1.38 Å. At low resolution (>1.9 Å), most of the measured phases in each of the images, except for a few weak reflections, were within 45° of the values calculated from the model and, when the constraint of 0 or 180° was imposed, agree with the model. Phase errors become significantly worse at higher resolution, as evidenced by the low figure-of-merit values for high-resolution reflections in Table 2. Deviations are largely due to slight local misorientation of the foil due to bending, to slight misalignment of the beam, and to contributions from non-linear interferences. Nine of the averaged phases in Table 2 disagree with those calculated from the model. Most of these are rather weak reflections in the model calculations. In several cases it is clear that non-linear effects are quite significant, as the amplitudes from the experimental images are strong. For example, the 020 reflections from [100] and [101] sections have high amplitudes, good figures of merit, but opposite phases. Closer inspection of these reflections in calculations from the model reveals a strong dynamical contribution which varies differently in different projections.

There is more spread among measured amplitudes and particularly between measured and calculated amplitudes (see also Fig. 7). This is not surprising because amplitudes are more influenced by non-linear terms. Since amplitudes generally affect fine details in refinements, whereas phases determine the major structural features (*e.g.* Ramachandran & Srinivasan, 1970, Fig. 1, p. 63), we were not greatly concerned about deviations in amplitudes at this stage. In principle, amplitudes could be determined from electron diffraction patterns, which are unaffected by the CTF. We have not used electron diffraction patterns because they average over large areas of varying thickness and are therefore subject to substantial dynamic

Table 2. *Averaged amplitudes and phases (°) for 59 reflections of staurolite*

These data were used for the reconstruction of the 3D Coulomb potential distribution. Amplitudes are corrected for the drop off of the envelope of the contrast transfer function. Experimental values in five different sections are compared with model values based on atomic parameters of Smith (1968). The figure of merit (f.o.m.) calculated from agreement within the through-focus series is indicated. Amp. = amplitude, Phs. = phase.

				[001]			[010]			[100]			[101]			[310]			Average			Model	
H	*K*	*L*	*d*	Amp.	Phs.	F.o.m.	Amp.	Phs.	F.o.m.	Amp.	Phs.	F.o.m.	Amp.	Phs.	F.o.m.	Amp.	Phs.	F.o.m.	Amp.	Phs.	F.o.m.	Amp.	Phs.
0	0	2	2.83				0.580	180	0.81	0.837	180	0.69				0.156	180	0.79	0.475	180	0.74	0.803	180
0	0	4	1.41							0.531	0	0.91				0.264	0	0.95	0.448	0	0.92	1.622	0
0	2	0	8.30	0.092	180	0.95				0.401	0	0.90	0.361	180	0.99				0.033	180	0.09	0.070	0
0	2	2	2.68							0.493	180	0.95							0.569	180	0.95	0.306	180
0	4	0	4.15	0.474	180	0.88				0.764	180	0.89	0.537	180	0.98				0.660	180	0.91	0.706	180
0	4	2	2.34							0.283	0	0.84							0.289	0	0.84	0.191	0
0	6	0	2.77	0.969	0	0.92				0.822	0	0.80	0.426	0	0.89				0.783	0	0.87	1.028	0
0	6	2	1.98							1.277	0	0.46							0.713	0	0.46	1.213	0
0	8	0	2.08	0.140	0	0.36				0.239	0	0.62	0.078	0	0.75				0.105	0	0.56	0.158	0
0	8	2	1.67							0.265	180	0.35							0.113	180	0.35	0.240	180
0	10	0	1.66	0.469	0	0.74				0.315	180	0.84	0.156	0	0.86				0.087	0	0.23	0.335	0
0	10	2	1.43							0.339	180	0.51							0.210	180	0.51	0.320	180
0	12	0	1.38	0.848	0	0.55				0.140	0	0.76	0.209	0	0.31				0.261	0	0.54	1.500	0
1	1	0	7.11	0.095	180	0.67													0.077	180	0.67	0.226	180
1	1	1	4.43										0.530	0	0.99				0.641	0	0.99	0.131	0
1	3	0	4.53	0.349	0	0.97										0.156	0	1.00	0.337	0	0.97	0.123	0
1	3	1	3.53										0.294	0	0.97	0.112	0	0.81	0.233	0	0.94	0.340	0
1	3	2	2.40													0.384	0	0.99	0.431	0	0.99	1.088	0
1	3	3	1.74													0.163	0	0.96	0.185	0	0.93	0.203	0
1	5	0	3.06	0.196	180	0.93													0.222	180	0.93	0.337	180
1	5	1	2.69										0.461	180	0.96				0.538	180	0.96	0.953	180
1	7	0	2.27	0.081	180	0.57													0.056	180	0.57	0.144	180
1	7	1	2.11										0.227	180	0.67				0.185	180	0.67	0.616	180
1	9	0	1.80	0.255	180	0.77													0.240	180	0.77	0.119	180
1	9	1	1.71										0.308	0	0.32				0.120	0	0.32	0.339	0
1	11	0	1.48	0.100	0	0.27													0.033	0	0.27	0.120	180
1	11	1	1.43										0.134	180	0.49				0.080	180	0.49	0.085	0
2	0	0	3.94	0.154	0	0.88	0.341	180	0.63										0.048	180	0.16	0.131	0
2	0	1	3.23				0.463	180	0.93										0.524	180	0.89	0.320	180
2	0	2	2.30				0.425	180	0.43				0.186	180	0.96				0.289	180	0.64	0.630	180
2	0	3	1.70				0.504	180	0.51										0.541	180	0.78	0.203	0
2	2	0	3.56	0.258	180	0.91													0.286	180	0.91	0.474	180
2	2	2	2.21										0.098	0	0.63				0.075	0	0.63	0.010	0
2	4	0	2.86	0.317	0	0.90													0.347	0	0.90	0.315	0
2	4	2	2.01										0.117	180	0.55				0.078	180	0.55	0.170	180
2	6	0	2.26	0.532	180	0.88										0.223	180	0.88	0.458	180	0.88	0.614	180
2	6	1	2.10													0.099	0	0.94	0.084	0	0.84	0.078	180
2	6	2	1.77										0.349	0	0.60	0.280	180	0.93	0.035	180	0.09	0.063	0
2	6	3	1.45													0.075	180	0.89	0.068	180	0.92	0.079	0
2	8	0	1.84	0.181	0	0.96													0.213	0	0.96	0.092	0
2	8	2	1.54										0.180	180	0.67				0.147	180	0.67	0.541	180
2	10	0	1.53	0.306	0	0.87													0.323	0	0.87	0.154	0
3	1	0	2.59	0.272	180	0.93													0.309	180	0.93	0.290	180
3	1	3	1.52										0.110	0	0.55				0.073	0	0.55	0.338	0
3	3	0	2.37	0.684	0	0.97													0.807	0	0.97	0.883	0
3	3	3	1.48										0.065	180	0.29				0.023	180	0.29	0.206	180
3	5	0	2.06	0.229	180	0.97													0.270	180	0.97	0.194	180
3	7	0	1.76	0.134	180	0.93													0.152	180	0.93	0.110	180
3	9	0	1.51	0.246	0	0.32													0.096	0	0.32	0.363	0
3	9	1	1.46													0.035	180	0.84	0.028	180	0.73	0.082	180
4	0	0	1.97	1.387	0	0.98	0.931	0	0.82										1.296	0	0.92	1.304	0
4	0	1	1.86				0.134	180	0.40										0.107	180	0.53	0.194	180
4	0	2	1.62				0.324	0	0.93										0.431	0	0.79	0.506	0
4	2	0	1.91	0.149	0	0.87													0.158	0	0.87	0.056	180
4	4	0	1.78	0.249	180	0.80													0.242	180	0.80	0.331	180
4	6	0	1.60	0.595	180	0.73													0.531	180	0.73	0.296	180
4	8	0	1.43	0.088	0	1.00													0.107	0	1.00	0.043	0
5	1	0	1.57	0.103	0	0.79													0.100	0	0.79	0.242	0
5	3	0	1.51	0.314	0	0.77													0.295	0	0.77	0.667	0

scattering (see § 4). Conceivably, convergent-beam microdiffraction could produce more accurate amplitude data, but these are difficult to correlate with a local area used for phase determination. After CTF envelope correction and final scaling of the five data sets, the R factor between experimental and model data was 29%.

Using the symmetry operations of the *Ccmm* space group, we expanded the 59 unique reflections to 162 structure factors in half space. With these structure factors F_{hkl}, given by amplitudes $|F_{hkl}|$ and phases φ_{hkl}, a three-dimensional electron potential map $V(x, y, z)$ can be reconstructed by a Fourier synthesis

$$V(x, y, z) = \sum |F_{hkl}| \exp 2\pi i \varphi_{hkl} \times \exp[-2\pi i(hx + ky + lz)]. \quad (5)$$

The summation is ideally over all reciprocal-lattice vectors *hkl*. In our case it is limited by the five sections and by resolution (1.38 Å).

Fig. 8(*a*) shows a solid-surface representation of the three-dimensional density map in stereoview, with a surface chosen to enclose all of the cations and associated O atoms that are present at full occupancy.

A full unit cell is shown; the view is oblique along the z axis. The tubular framework represents cations bonded to surrounding O atoms to form octahedra and tetrahedra which are linked, and can be compared with an *ORTEP* plot of the crystal structure (Fig. 8*b*). Many of the details are easier to see in two-dimensional sections. Since all atoms are located near planes with $z=0$ and $z=\frac{1}{4}$, and because of the assumed orthorhombic symmetry, most of the information is contained in $xy0$ and $xy\frac{1}{4}$ sections (Fig. 9). For comparison, reconstructions of the [001] projections are added (Fig. 9, top). Gray shades correspond to the electron potential which allows one to estimate atom location and identity. The potential distribution is shown for three reconstruction models: Fig. 9(*a*) is the potential map for only 30 reflections using a single image at Scherzer focus from each projection

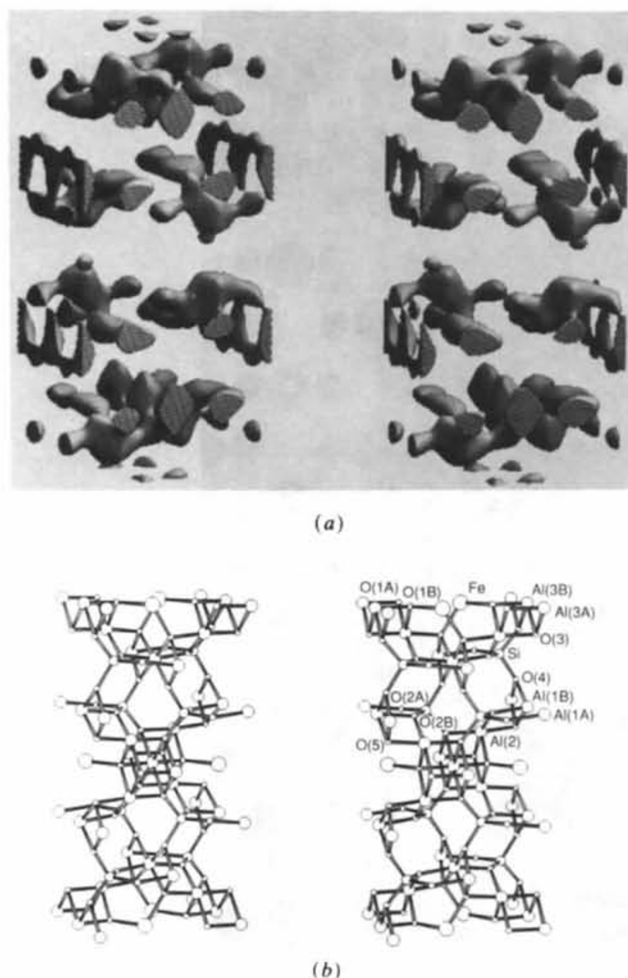

Fig. 8. Stereopairs of the 3D Coulomb potential of staurolite for a full unit cell. (*a*) Experimental contour surface shown to include all fully occupied cations and O atoms. Structure calculated from data in Table 2. (*b*) Corresponding *ORTEP* plot of the crystal structure of staurolite with atoms labeled and metal-oxygen bonds indicated. View is oblique along **z**.

and to a resolution of 1.68 Å which has been reported previously (Downing *et al.*, 1990). Fig. 9(*b*) is the reconstruction from 59 reflections to a resolution of 1.38 Å and using data from a focus series in each projection with the amplitudes not corrected for the falloff of the CTF envelope. Fig. 9(*c*) is derived from the same data but with a CTF envelope correction. Fig. 9(*d*) illustrates the crystal structure based on Smith's (1968) model with the locations of all atoms indicated.

As expected, the map is not much improved by adding the raw image data between 1.68 and 1.38 Å, due to the low structure-factor amplitudes. Also, the resolution is markedly improved by compensating for the CTF envelope falloff. We find a good correspondence between model and experiment, with all atoms clearly resolved. The partially occupied Al(3) site has a much lower potential than fully occupied Al(1) and Al(2) sites. Due to the high three-dimensional resolution, all O atoms – those associated with octahedra (Al-O = 2.2 Å) and those associated with tetrahedra (Fe-O = 2.0, Si-O = 1.65 Å) – can be clearly distinguished. In tetrahedra, due to short T-O distances, there is more overlap between cations and O atoms, particularly in the $z=\frac{1}{4}$ section. Note that in neither of the two sections are there erroneous potential peaks not associated with atoms.

It is revealing that the reconstruction with 59 reflections obtained to a resolution of 1.38 Å from many focus conditions is only moderately better than the 30 reflection model to a resolution of 1.68 Å using only images close to Scherzer. Improvements are mainly seen for Si and O atoms in the $z=\frac{1}{4}$ section but note that the occupancy for Fe atoms is worse in the 1.38 Å model. Since interatomic distances in minerals and ceramics are rarely less than 1.6 Å, a corresponding resolution, which can be achieved with the simple Scherzer model, may be sufficient for many applications.

7. Discussion

With the example of staurolite we demonstrate that 3D electron crystallography is a feasible method for crystal structure analysis on an atomic scale. If thin foils are used, errors introduced by dynamic scattering are less serious than generally assumed and, in particular, phases are not appreciably affected. To our knowledge this is the first example where O atoms have been directly resolved with electron-microscope methods. The big improvement over protein structure determinations was possible because of the availability of high-resolution images with a point-to-point resolution of better than 2 Å, which is a typical cation–oxygen distance in many silicates and oxides. Locating atoms appears to be straightforward by this method. It may be more difficult to assign atomic species in the case of an unknown structure because

of experimental and theoretical limitations. It is noteworthy that 3D crystal structures have been determined from electron diffraction data, using exclusively intensities and proceeding along similar lines as in X-ray crystallography. Atomic resolution was obtained for example for clay minerals (Zvyagin, 1967). The main difference of the present method is that it directly determines phases from high-resolution images.

The advantages of 2D sections over projections of 3D structures can be seen by comparing weak-phase-object 'maps' simulated by using all reflections within a given resolution range (Fig. 10). These maps were calculated from model sections consisting of a single layer of atoms either at $z = 0$ or at $z = \frac{1}{4}$ and therefore display an artificial 'infinite' resolution along **z**. In the 2D [001] projection, atoms are not resolved, even at 1.4 Å resolution. This lack of resolution is due to overlaps, and is illustrated in the atom model in Fig. 9(*d*) (top). In sections of the 3D structure, however, O atoms in the *xy*0 section become resolved at a resolution of 2 and 1.8 Å with only moderate improve-

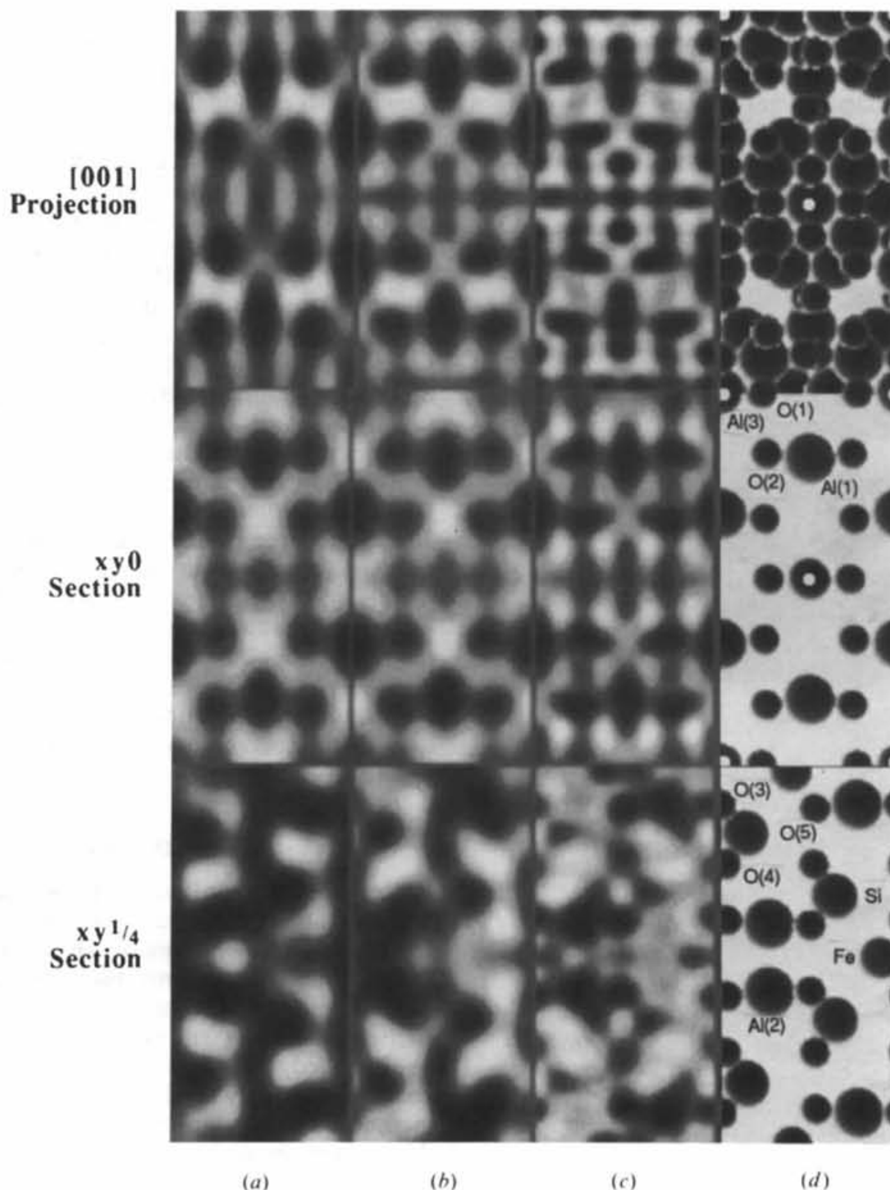

Fig. 9. [001] projection and *xy* sections through the structure of staurolite at $z = 0$ and $z = \frac{1}{4}$. Gray shades indicate densities. (*a*) Reconstruction of Coulomb potential from 30 reflections obtained from five images at Scherzer focus to a resolution of 1.68 Å (Downing *et al.*, 1990). (*b*) Reconstruction of the Coulomb potential with 59 independent reflections, averaged from five through-focus series of images, to a resolution of 1.38 Å. (*c*) Same as (*b*) but with a correction for the CTF envelope drop off with resolution. (*d*) Atom positions based on the model of Smith (1968).

ment at higher resolution. In the $xy\frac{1}{4}$ section, O atoms associated with Si tetrahedra become distinct only beyond 1.6 Å resolution due to the short Si–O distance of 1.65 Å.

If we compare 2D projections of experimental reconstructions (Figs. 9*a*–*c*) and simulations (Fig. 10). it is apparent on visual inspection that the resolution of the experimental 30 reflection model corresponds to 2 Å, that of the uncorrected 59 reflection model to 1.8–1.6 Å and that of the CTF-corrected 59 reflection model to 1.4 Å. The uncorrected model shows lower resolution because high-resolution reflections contribute less to the reconstruction. In the 3D sections the resolution of the 30 reflection model (Fig. 9*a*) is 2 Å; that of the uncorrected 59 reflection model is similar (Fig. 9*b*). Resolution of the 59 reflection CTF-corrected model is about 1.8 Å. There are two main reasons for the poor comparison of 3D sections. Firstly, $xy0$ and $xy\frac{1}{4}$ layers in the structure are spaced by only 1.4 Å and the idealized section simulations with single-atom layers are somewhat unrealistic because they assume a resolution much better than this in the z direction. In the 59 reflection CTF-corrected model we can see, for example (Fig. 9*c*, center), elongated tails in the Al atoms in the $xy0$ section, which are caused by O atoms in the adjacent

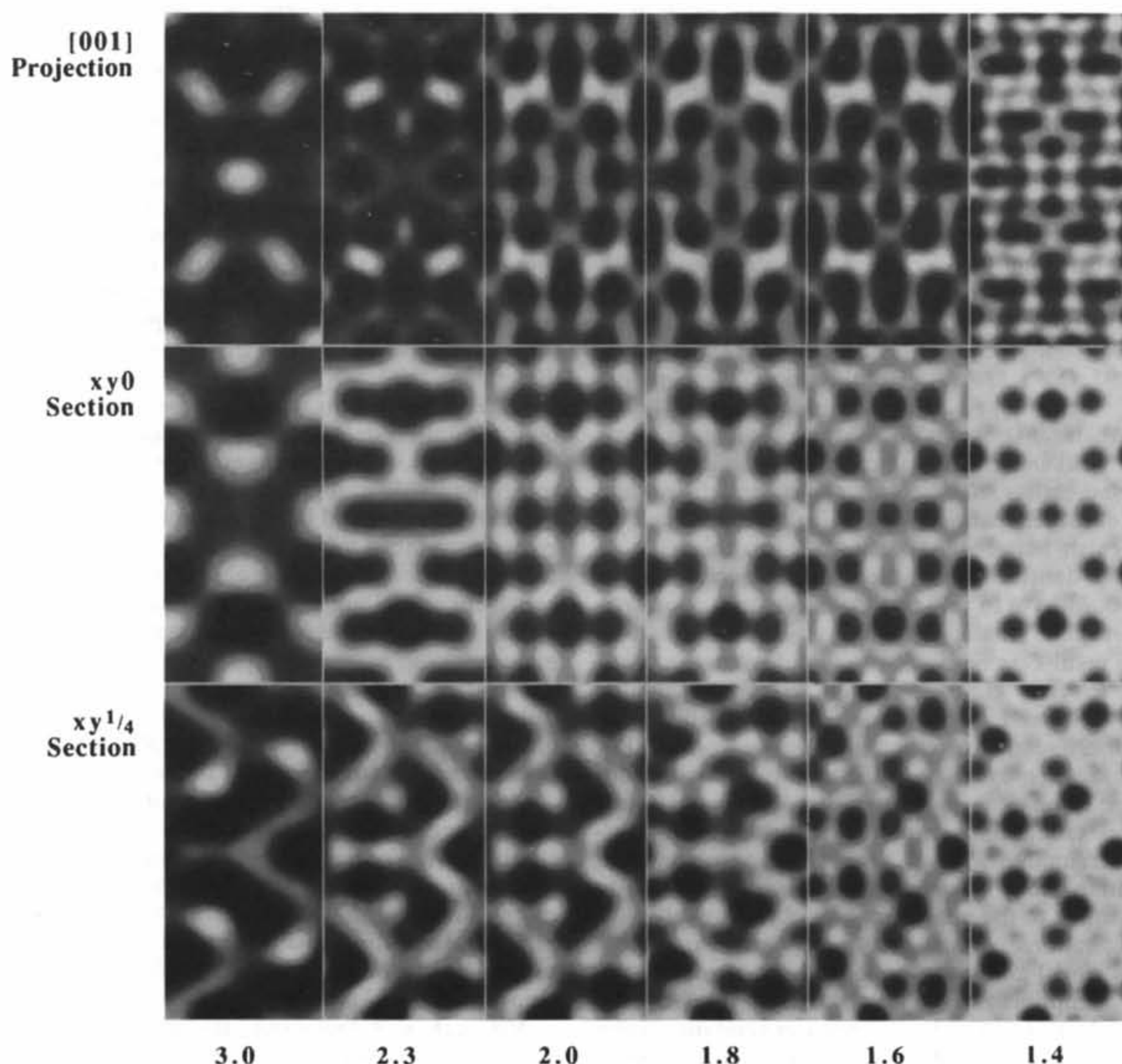

Fig. 10. Simulations of staurolite in [001] orientation under weak-phase-object (WPO) conditions computed from the theoretical potential and not considering microscope aberrations. Resolutions marked in Å for the full unit-cell projection (top) and sections at $xy0$ and $xy\frac{1}{4}$. Overlapping atoms in the full unit-cell projection prevent unambiguous identification of individual atoms even at resolution as high as 1.4 Å. On the other hand, in the $xy0$ and $xy\frac{1}{4}$ sections, the cations and anions are clearly resolved even at 1.8 and 1.6 Å resolution, respectively. Comparison of simulated projections with experimental results of Fig. 9 demonstrates that a WPO resolution of 1.4 Å was achieved in the final 3D reconstruction.

$xy\frac{1}{4}$ layer. In our data set there is only one reflection with an l index of 4 (resolution 1.4 Å) and five with an l index of 3 (resolution 1.86 Å) which are clearly insufficient to provide a complete separation of the $xy0$ and $xy\frac{1}{4}$ sections.

The second reason for discrepancies between simulations and experimental reconstructions is incomplete sampling of reciprocal space. Even within the resolution range to 1.38 Å, 34 non-extinct reflections were omitted in our five sections, including strong reflections such as 221, 241, 311, 223, 153, 282, 313, 192, 511, 173 and 462 (*e.g.* Náray-Szabó, 1929). These Fourier components, some at low resolution and all with general indices *hkl*, are important for locating atoms which are not in special positions such as Si and Al near the $z=\frac{1}{4}$ layer. Addition of high-resolution Fourier terms in the five observed sections does not compensate for the lack of these data. It may explain why Fe, for example, shows such a low density. Contributing to errors is a slight bending of the foil, which is impossible to avoid, and a low signal-to-noise ratio.

Electron scattering factors are more uniform than X-ray scattering factors and do not vary monotonically with atomic number which makes it more difficult to identify atomic species. For example, electron scattering amplitudes are Fe = 2.93, Al = 1.74, Si = 1.97, O = 1.22 Å at a resolution of 2 Å (*International Tables for X-ray Crystallography*, 1974). Nevertheless, O atoms in the potential maps show much weaker densities than cations, and partially occupied cation sites also have a lower density than fully occupied cation sites. It is more difficult to distinguish between Al, Si and Fe on the basis of potential densities, and if the structure were unknown one would have to rely on inferences from coordination and interatomic distances.

The results do not look very good when the traditional R-factor criterion is used. We obtain a value for R (observed *versus* model) of 29% even though the experimental structure is basically correct. But the R factor only assesses the quality of amplitudes and not of phases which are more significant in electron crystallography and for determining atom positions. Compared with an X-ray structure refinement, resolution from electron crystallography is clearly inferior due to the poor sampling of reciprocal space [59 reflections *versus* 3160 reflections in Smith's (1968) work] and also due to higher errors in determining amplitudes.

But 3D atomic-resolution electron crystallography as introduced here opens a new dimension for crystal structure determinations. One advantage over X-rays is that phases can be determined experimentally with good reliability at least up to a resolution of about 1.4 Å, which is sufficient to resolve the locations of atoms. A second advantage is that structure determinations can be done on very small volumes, only a few unit cells wide. Many minerals and ceramics are heterogeneous on a submicroscopic scale due to phase transformations or growth defects. Examples of systems in which local structures are still uncertain are rhombohedral carbonates, plagioclase feldspars of intermediate composition, some pyroxenes and perovskite-related structures. All present information relies on averages over the matrix and the domains which are of interest.

There are several requirements for high-resolution electron crystallography:

(1) The material to be analyzed should be stable in the electron beam, preferably so that through-focus series can be taken in the same area in different directions. In case of very beam-sensitive materials, similar methods could be employed as in protein microscopy with sample cooling and low-dose imaging (Henderson & Unwin, 1975).

(2) The higher the resolution of the electron microscope the better is the structure determination. With conventional microscopes and 3 Å point-to-point resolution, general features can be distinguished but individual atoms cannot be resolved. Atomic resolution becomes possible with 2 Å but is improved with 1.4 Å resolution which we had available with the ARM-1000. It is particularly important to have tilting capability to image the structure in different directions.

(3) HREM negatives need to be digitized with a high-resolution densitometer or enlarged images can be digitized with a scanner. Alternatively, direct recording with a digitizing CCD (charge-coupled device) camera could be used which would eliminate errors introduced by the non-linear response of films. It is also necessary to have access to an optical laser bench for a preliminary survey of the image to find a thin area in proper orientation, to evaluate astigmatism and to ascertain Scherzer focus. The latter is one of the most difficult aspects, particularly if the foil is inclined to the beam so that the focus which has been determined for the amorphous edge does not correspond to the area of interest.

(4) Much of the analysis relies on computer processing and availability of corresponding software; specifically, Fourier transformations of digitized images and windowing (*e.g.* Hovmöller, Sjögren, Farrants, Sundberg & Marinder, 1984; Saxton, 1986), phase and amplitude extraction, determination of the proper phase origin and finally three-dimensional reconstruction (Amos *et al.*, 1982).

Although still laborious, the general method is remarkably simple and robust because very few assumptions are made. It is unnecessary, for example, to constrain the crystal symmetry even though this may be helpful in determining the phase origin. We have chosen a known crystal to demonstrate the method, but we really only used the structure information in the final comparison. A better sampling of

reciprocal space could be achieved by tilting foils to more different orientations. Interestingly, the crude model using only 30 reflections from images at Scherzer focus and without CTF correction was interpretable in terms of the model structure. For a quick determination of the main features of the crystal structure the simple procedure may be adequate. It is conceivable that 3D electron crystallography could be combined with an X-ray structure determination. Electron crystallography could provide a first phase model from which the structure could be further refined with X-ray amplitude data.

We have mentioned above that, while amplitudes are very susceptible to thickness and focus changes, phases are more stable, at least for centrosymmetric crystals. This can be used for space-group determination in cases where the space group is ambiguous from diffraction patterns. This point deserves some elaboration.

The wave function $\Phi(u)$ in reciprocal space (or the image-amplitude spectrum) is given by the expression

$$\Phi(u) = \sum_g \Psi(u) \exp[-i\chi(u)]\delta(u-g)A(u) \quad (6)$$

where $\Psi(u)$ is the wave function of the crystal in reciprocal space, $\exp[-i\chi(u)]$ is the change in the phase of the wave function that is caused by defocus and spherical aberration, $\delta(u-g)$ is a δ function and $A(u)$ is the objective aperture function. We write for an individual term in the image-amplitude spectrum

$$\psi(u) = \Psi(u) \exp[-i\chi(u)]A(u). \quad (7)$$

For a centrosymmetric crystal,

$$\Psi(u) = \Psi(-u) \quad (8)$$

and

$$\Phi(u) = \sum_g \psi(u)\delta(u-g). \quad (9)$$

The inverse Fourier transform of $\Phi(u)$ is the wave function of the image, that is

$$\Psi_i(x) = \mathscr{F}^{-1}[\Phi(u)]. \quad (10)$$

The intensity of the image $I(x)$ can be represented by the product of the wave function and its complex conjugate

$$I(x) = \Psi_i(x)\Psi_i(x)^*. \quad (11)$$

The forward Fourier transform of $I(x)$ is the wavefunction $\Phi_{od}(u)$ of the optical diffractogram (computed transform), that is

$$\Phi_{od}(u) = \mathscr{F}[I(x)]. \quad (12)$$

For $u = g$, $\Phi_{od}(g)$ can be represented by the expression

$$\Phi_{od}(g) = \sum_{g'} \psi(g+g')\psi^*(g'). \quad (13)$$

The optical diffractogram is two-dimensional, $g = (H, K)$. If at least one of H and K is odd, then

$$\Phi_{od}(g) = [\psi(g+g_1)\psi^*(g_1) + \psi(-g_1)\psi^*(-g_1-g)] + [\psi(g+g_2)\psi^*(g_2) + \psi(-g_2-g)] + \ldots.$$

From $\psi(u) = \psi(-u)$,

$$\begin{aligned} \Phi_{od}(g) &= [\psi(g+g_1)\psi^*(g_1) + \psi(g_1)\psi^*(g_1+g)] \\ &\quad + [\psi(g+g_2)\psi^*(g_2) + \psi(g_2+g)] + \ldots \\ &= \mathrm{Re}\,[\psi(g+g_1)\psi^*(g_1)] \\ &\quad + \mathrm{Re}\,[\psi(g+g_2)\psi^*(g_2)] + \ldots \\ &= \sum_{g'} \mathrm{Re}\,[\psi(g+g')\psi^*(g')]. \end{aligned} \quad (14)$$

If both H and K are even,

$$\Phi_{od}(g) = \sum_{g' \neq g/2} \mathrm{Re}\,[\psi(g+g')\psi^*(g')] + \psi(g/2)\psi^*(g/2). \quad (15)$$

As long as the central beam is strong, *i.e.* the foil is not too thick, $\mathrm{Re}\,[\psi(g)\psi^*(g_0)]$ is predominant in the summation of (14) and (15). From (7), the sign of $\Phi_{od}(g)$ is dependent on

$$\mathrm{Re}\,\{\Psi(g) \exp[-i\chi(g)]A(g) \times \Psi^*(g_0) \exp[i\chi(g_0)]A(g_0)\}.$$

Therefore, for a pair of reflections hkl and $h\bar{k}\bar{l}$, phases and amplitudes of Φ_{od} are susceptible to defocus and thickness, but their phase relation is independent of defocus and thickness of crystal, *i.e.* the symmetry is maintained. Thus the phase relation of the wave function $\Phi_{od}(g)$ is the same as that of the wave function $\Psi(g)$ of the crystal in reciprocal space. For example, if the signs of $\Psi(hkl)$ and $\Psi(h\bar{k}\bar{l})$ are opposite, the wave function Φ_{od} in the optical diffractogram will have the same relation, that is, the phases of $\Phi_{od}(hkl)$ and $\Phi_{od}(h\bar{k}\bar{l})$ are opposite under any defocus and thickness. For example, we can see in Fig. 6 that the phases of symmetry-related reflections change with focus and thickness by the symmetry relationship does not change. Thus, space-group determination for centrosymmetric crystals can be done by processing HREM images which are not taken at Scherzer defocus and not from very thin areas of a crystal. There are numerous examples of space-group ambiguities, perhaps most belabored in perovskite-type structures.

The aforegoing discussion also implies that phases could be determined in thicker areas as long as all reflections are from the same thickness or are normalized to the same thickness. This simple behavior does of course not hold for noncentric crystals.

In conclusion, we wish to emphasize again the great potential of 3D electron crystallography for structure determinations, particularly in heterogeneous materials. This first example was a rather rough test

and did not unravel any new features of the staurolite structure. Instead, the X-ray structure was confirmed. In the future, procedures can be refined and become more routine as the method is applied to other examples with known structure to test the reliability and to unknowns.

HRW remembers a PhD qualifying examination in the Department of Biophysics and following discussions with Professor R. Glaeser which initiated this interdisciplinary research. J. Arnoth supplied the specimen of staurolite and A. C. Larson kindly helped with the stereoplot. Comments from two reviewers improved the manuscript. Financial support from NSF Grants EAR-88 16577 and 91 04605 (to HRW), NIH Grant GM-36884 (to KHD) and from the UC Education Abroad Program (to HM and HRW) is gratefully acknowledged. KHD is supported by the Assistant Secretary of the Office of Environmental and Health Research, Office of Energy Research, MAO'K and NCEM are supported by the Director, Office of Basic Energy Sciences, Materials Science Division, all through the US Department of Energy under Contract No. DE AC-03-76SF0098. HRW and HM are grateful for generous access to facilities at NCEM and for assistance by C. Nelson and D. Ah Tye. HRW is appreciative of the hospitality at CMS LANL on the occasion of a leave.

References

AMOS, L. A., HENDERSON, R. & UNWIN, P. N. T. (1982). *Prog. Biophys. Mol. Biol.* **39**, 183-231.
BRILLINGER, D. R., DOWNING, K. H. & GLASSER, R. M. (1990). *J. Stat. Plan. Inference*, **25**, 235-259.
DE ROSIER, D. J. & KLUG, A. (1968). *Nature (London)*, **217**, 130-134.
DE ROSIER, D. J. & MOORE, P. B. (1970). *J. Mol. Biol.* **52**, 355.
DOWNING, K. H., HU, M., WENK, H.-R. & O'KEEFE, M. A. (1990). *Nature (London)*, **348**, 525-528.
EPICIER, T., O'KEEFE, M. A. & THOMAS, G. (1990). *Acta Cryst.* **A46**, 948-962.
FRANK, J. (1973). *Optik (Stuttgart)*, **38**, 519-536.
GLAESER, R. M. (1985). *Ann. Rev. Phys. Chem.* **36**, 243-275.
GRONSKY, R. (1980) *38th Ann. Proc. Electron Microsc. Soc. Am.* San Francisco Press.
HAINISCH, K. (1966). *N. Jb. Mineral. Monatsh.* pp. 362-366.
HENDERSON, R., BALDWIN, J. M., CESKA, T., ZEMLIN, F., BECKMANN, E. & DOWNING, K. H. (1990). *J. Mol. Biol.* **213**, 899-929.
HENDERSON, R. & UNWIN, P. N. T. (1975). *Nature (London)*, **257**, 28-32.
HETHERINGTON, C. J. D., NELSON, E. C., WESTMACOTT, K. H., GRONSKY, R. & THOMAS, G. (1989). *Mater. Res. Soc. Symp. Proc.* **139**, 277-282.
HOVMÖLLER, S., SJÖGREN, A., FARRANTS, G., SUNDBERG, M. & MARINDER, B. O. (1984). *Nature (London)*, **311**, 238-241.
International Tables for Crystallography (1989). Vol. A. Dordrecht: Kluwer Academic Publishers.
International Tables for X-ray Crystallography (1974). Vol. IV, Table 2.4.6A, p. 155. Birmingham: Kynoch Press. (Present distributor Kluwer Academic Publishers, Dordrecht.)
JACOB, J. (1941). *Schweiz. Mineral. Petrogr. Mitt.* **21**, 124.
JUURINEN, A. (1956). *Ann. Acad. Sci. Fenn. Ser. A* 3, **47**, 1-53.
KILAAS, R. (1987). *45th Ann. Proc. Electron Microsc. Soc. Am., Baltimore*, pp. 66-69. San Francisco Press.
MEIKE, A., WENK, H.-R., O'KEEFE, M. A. & GRONSKY, R. (1988). *Phys. Chem. Miner.* **15**, 427-437.
NÁRAY-SZABÓ, I. (1929). *Z. Kristallogr.* **71**, 103-116.
NÁRAY-SZABÓ, I. & SASVÁRI, K. (1958). *Acta Cryst* **11**, 862-865.
O'KEEFE, M. A. (1979). *37th Ann. Proc. Electron Microsc. Soc. Am., San Antonio, TX*, pp. 556-557. Baton Rouge: Claitor.
O'KEEFE, M. A., BUSECK, P. R. & IIJIMA, S. (1978). *Nature (London)*, **274**, 322-324.
RAMACHANDRAN, G. N. & SRINIVASAN, R. (1970). *Fourier Methods in Crystallography.* New York: Wiley.
SAXTON, W. O. (1986). *44th Ann. Proc. Electron Microsc. Soc. Am., San Francisco*, pp. 526-529. San Francisco Press.
SMITH, D. J., CAMPS, R. A., FREEMAN, L. A., O'KEEFE, M. A., SAXTON, W. O. & WOOD, G. J. (1985). *Ultramicroscopy*, **18**, 63-76.
SMITH, J. V. (1968). *Am. Mineral.* **53**, 1139-1155.
STOUT, G. H. & JENSEN, L. H. (1989). *X-ray Structure Determination. A Practical Guide.* New York: Wiley.
TAKÉUCHI, Y. & AIKAWA, N. (1972). *Z. Kristallogr.* **136**, 1-22.
VEBLEN, D. R. & BUSECK, P. R. (1979). *Science*, **206**, 1398-1400.
WENK, H.-R. (1980). *Am. Mineral.* **65**, 766-769.
ZVYAGIN, B. B. (1967). *Electron Diffraction Analysis of Clay Mineral Structures.* New York: Plenum.

Acta Cryst. (1992). A**48**, 716-727

The Domain Matrix Method: a New Calculation Scheme for Diffraction Profiles

BY S. PFLANZ AND W. MORITZ

Institut für Kristallographie und Mineralogie der Universität, Theresienstrasse 41, D-8000 München 2, Germany

(*Received* 25 *October* 1991; *accepted* 10 *March* 1992)

Abstract

A new calculation scheme for diffraction profiles is presented that combines the matrix method with domain approaches. Based on a generalized Markov chain, the method allows the exact solution of the diffraction problem from any one-dimensionally disordered domain structure. The main advantage of this

0108-7673/92/050716-12$06.00 © 1992 International Union of Crystallography